Effects of calcination on microscopic and mesoscopic structures in Ca- and Sr-doped nano-crystalline lanthanum chromites

Himal Bhatt [a,*], J. Bahadur [b], M.N. Deo [a], S. Ramanathan [c], K.K. Pandey [a], D. Sen [b], S. Mazumder [b], Surinder M. Sharma [a]

[a] High Pressure and Synchrotron Radiation Physics Division, Bhabha Atomic Research Centre, Trombay, Mumbai 400085, India
[b] Solid State Physics Division, Bhabha Atomic Research Centre, Trombay, Mumbai 400085, India
[c] Materials Processing Division, Bhabha Atomic Research Centre, Trombay, Mumbai 400085, India

ARTICLE INFO

ABSTRACT

Calcination behavior of nano-crystalline lanthanum chromites doped with calcium and strontium has been probed by Fourier transform infrared spectroscopy, X-ray diffraction and small-angle neutron scattering as a function of temperature. Infrared spectroscopic results imply that over a range of temperatures, some intermediate phase of dopant chromates evolve and then dissolve back, which has also been confirmed by the XRD. Neutron scattering data reveal a fractal type correlation of building blocks in virgin powders. Increase in fractal dimension and reduction in upper cutoff vis-à-vis the densification of agglomerates were found with increasing calcination temperature. Calcination, beyond 900 °C, results in breaking down of the fractal morphology almost completely. Such shrinkage event also results in a modification of the microscopic structure. These changes have been attributed to the compaction of agglomerates of both Ca- and Sr-doped lanthanum chromites, assisted via liquid state sintering by the melting of the intermediate phases at intermediate calcination stages.

1. Introduction

In recent past, a lot of studies [1–5] have been devoted to solid oxide fuel cells (SOFC), a potential candidate for distributed generation, due to its capability of power production at high efficiencies, fuel flexibility and long-term stability. But, still there are concerns over the issues related to the physico-chemical properties of its components at high temperatures, as SOFC is generally operated at temperatures ranging around 850–1000 °C. The three basic components of a SOFC are the ionic electrolyte, two porous electrodes and interconnect that sits between each individual cells to provide an electrical pathway from anode of one cell to cathode of the adjacent cell. There are various requirements for making the interconnects viz. the material should have good chemical stability in oxidizing as well as in reducing atmospheres, high electrical conductivity, compatibility of thermal expansion behavior with other components of the cell, high density to avoid material deposition at high temperatures and good mechanical strength at high temperatures. Stoichiometric lanthanum chromite perovskites, $LaCrO_3$, are known to show excellent chemical stability under oxidizing or reducing atmospheres at high temperature, but exhibit poor sintering in air and low electrical conductivity at SOFC

operating temperatures [5–8]. This is due to the fact that chromium vapor component starts evaporating at temperatures beyond 1000 °C [9,10], thus disturbing the densification of lanthanum chromite particles by vaporization–condensation transport mechanism. Doping of alkaline earth metals like Sr and Ca in $LaCrO_3$ has shown to improve the sintering properties, apart from retaining all the stringent requirements of a SOFC interconnect [5,11]. Nearly 20 mol% of Sr doping and 30 mol% of Ca doping have been explored extensively as they provide reasonably optimum properties considering all the rigorous requirements of the interconnect [3,8,11–18]. During calcination of doped lanthanum chromites, mesoscopic structure and dynamics get modified with calcination temperatures. However, the possibility of new phase formation may not be ruled out. In a recent study on underdoped and overdoped $La_{0.7}Ca_xCrO_3$, it was noticed that a transient liquid phase formed between 850 and 1000 °C causing a partial densification [11]. Similar studies on $(La_{0.7}Sr_{0.3})_xCrO_3$ have also been carried out [14]. However, the issues related to achievement of highly sintered material at lower temperatures, which fulfills the requirements, still require attention. Consequently, the mesoscopic structure, governing the sintering and microscopic structure, governing the properties of the system must be discussed. Structural as well as spectroscopic information facilitates the exploration of the calcination behavior. In this regard, Fourier transform infrared spectroscopy (FTIR), X-ray diffraction (XRD) and small-angle neutron

* Corresponding author. Fax: +91 22 25505296.
E-mail addresses: himalphy@gmail.com, hbhatt@barc.gov.in (H. Bhatt).

scattering (SANS) are useful techniques to probe the calcination behavior.

Vibrational spectroscopy is an established technique to study the microscopic structures of the unit cell as particular motions of atoms are probed for different phonon modes and different phases formed during calcination by probing the fingerprint vibrations of various bonds present therein. Usually there are three kinds of phonon vibration modes in LaCrO$_3$ perovskites. La site external modes and internal CrO$_6$ octahedral distortions consisting of Cr–O–Cr bending modes and Cr–O stretching modes. Various infrared and Raman active phonon vibrational modes for LaCrO$_3$ have been reported in literature [18–20]. Detailed group theoretical calculations on perovskite structured compounds with *Pnma* phase have also been performed [21]. Doping induced disorder due to the changed mass, charge and lattice parameters broadens the bands. Substitution of divalent cations Sr^{2+} and Ca^{2+} in place of trivalent La^{3+} in the perovskite may be accompanied by a variation in the internal as well as external modes in terms of shifts in peak positions, widths and appearance of new modes, etc. It is worth mentioning here that the structure of the *ABO*$_3$ perovskite is such that they form two polyhedra AO$_{12}$ and BO$_6$, i.e. LaO$_{12}$ and CrO$_6$ in LaCrO$_3$. Vibrational spectroscopy is highly sensitive to any kind of volumetric changes in ABO$_3$ perovskite due to the deformation of these polyhedral via variation of their bond lengths ($d_{\text{La–O}}$ and $d_{\text{Cr–O}}$) and bond angles ($\theta_{\text{O–Cr–O}}$) [18].

In general, synthesis of nano-ceramics by gel-combustion method results into agglomerates of nano-particles and the sintering of agglomerates are accompanied by a modification in the mesoscopic structure [22–25]. Sintering of nano-particles has gained attention in recent years as better sintering properties can be obtained by using nano-phase material [23,25]. It is noted that calcination of the ceramics at higher temperatures is an effective method to achieve sintered material. Agglomerates in nano-ceramics may be represented in various situations by fractals. SANS is a well-established nondestructive technique to study fractal morphology in various materials in mesoscopic length scale [26,27] and has an advantage over mercury intrusion porosimetry [28,29]. It can probe both open and close pores in solids. The mathematical relation characterizing a fractal aggregate of radius R and mass M is given by $M(R) \propto R^{D_f}$, where D_f is the fractal dimensionality of the system [30], different from its normal Euclidean dimension. In reality, fractal nature of the aggregate is valid within some limited length scales, namely lower and upper cutoff. The scattered intensity, $I(q)$, at high enough wave-vector transfer q region varies as q^{-D_F} for mass or volume fractal objects within its cutoff lengths. The fractal dimension is also a quantitative measurement of the compactness of agglomerates. For compact and dense agglomerates, D_F is close to its Euclidean dimension. Scattering contributions from nano-phase structures are concentrated at small scattering angles. Scattering of neutrons in small-angle regime occurs if coherent scattering length density of the inhomogeneities is different from that of the medium. In case of porous solids, pores can be thought of as inhomogeneities and small-angle scattering of neutrons arises due to scattering contrast between the pores and the surrounding solid matrix [31–33].

The present work deals with the effects of the calcination temperatures on gel-combustion synthesized nano-crystalline La$_{0.7}$Ca$_{0.3}$CrO$_3$ (LCC) and La$_{0.8}$Sr$_{0.2}$CrO$_3$ (LSC) investigated by FTIR, XRD and SANS. Infrared spectroscopy has been utilized to monitor the behavior of infrared active modes and see the evolution of intermediate phases formed at different calcination temperatures, which has been complimented by the X-ray diffraction studies. Structural characterization by SANS has been performed in order to track the evolution of the mesoscopic structure with calcination temperature. A comparison has also been elucidated for the LCC and LSC at different calcination temperatures. The main goal of this paper is to expand our knowledge on these nano-phase compounds and provide more information on the influence of calcination temperatures.

2. Experiment

2.1. Sample preparation

An aqueous solution of nitrates of lanthanum, chromium, calcium or strontium corresponding to the composition La$_{0.7}$Ca$_{0.3}$CrO$_3$ (LCC) and La$_{0.8}$Sr$_{0.2}$CrO$_3$ (LSC) was obtained from stock solutions of individual metal nitrates. Stoichiometric amount of citric acid required for combustion was dissolved in the mixed solution. The solution was evaporated overnight to form into a dried gel at 80 °C in air oven. The oven dried gel was subjected to smooth combustion on a laboratory heater to form into a porous powder mass. The resulting powder was dried and wet ground in a planetary mill to a fine mass and has been denoted as 'as-prepared' specimen in the forthcoming text. Powder samples were calcined at varying temperatures in the range 600–1200 °C in a programmable laboratory kanthal furnace for 1 h to tailor their pore structure. In the present work, the effects of calcination have been probed on the final sintered specimens at different temperatures. As-prepared as well as powders calcined at 600, 900 and 1200 of LCC and LSC have been taken for infrared absorption, X-ray diffraction, small angle neutron scattering and scanning electron microscopy experiments.

2.2. Microscopic characterization

Infrared experiments have been performed on as-prepared as well as calcined LCC and LSC powders, using FTIR in transmission mode under vacuum. Infrared spectra in the spectral range 150–700 cm^{-1} have been recorded using BOMEM DA8 FTIR spectrometer with the co-addition of 100 scans at an apodized resolution of 2 cm^{-1}, using Globar source, 3 µm Mylar beamsplitter and DTGS (FAR-IR) detector. To check for the reproducibility of the spectra and expand the frequency range, measurements have been repeated in the spectral range 400–1500 cm^{-1} using Bruker Vertex 80V FTIR spectrometer at an apodized resolution of 2 cm^{-1}, using Globar source, KBr beamsplitter and DTGS (MID-IR) detector. A total of 50 scans have been co-added to get the desired spectra. For recording the infrared spectra, sample powders have been palletized with samples dispersed in CsI matrix. Background spectrum using bare CsI pallet has been divided in each case to obtain the transmission spectrum, denuded from instrumental and environmental profiles. The spectra were analyzed using ORIGIN and OPUS [34]. All experiments were performed at room temperature. Results of the measurements using the two spectrometers are highly reproducible in the overlap region. XRD patterns of the powders were recorded using a rotating anode X-ray generator equipped with Mo source. Data were collected using a Mar345 imaging plate and the images were converted into 1D diffraction patterns using FIT2D software. GSAS software was used for structural refinement.

2.3. Mesoscopic characterization

SANS experiments have been performed on the as-prepared as well as calcined powders, using a double crystal based medium resolution small angle neutron scattering instrument (MSANS) at Guide Tube Laboratory of the Dhruva reactor at Trombay, India [35]. The instrument consists of a non-dispersive $(1, -1)$ setting of $(1\,1\,1)$ reflections from silicon single crystals with specimen between two crystals. Scattered intensities have been recorded as a function of modulus of wave vector transfer $|q|$ $(=4\pi \sin(\theta)/\lambda$, where 2θ is the scattering angle and λ $(=0.312$ nm) is incident

neutron wavelength for present experiment). SANS profiles of specimens, recorded by the instrument, were corrected for smearing effect after transmission and background corrections, using the methods given in literatures [36,37]. Scanning electron microscopy (SEM) experiments have been performed to support the mesostructural observations.

3. Results and discussion

The X-ray diffraction patterns of LCC and LSC samples have been shown in Figs. 1 and 2, respectively. It is interesting to see that the XRD patterns for both the as-prepared powders are almost identical. This leads to iso-structural crystalline phase of both LCC and LSC. The XRD data have been used for structural refinement, which has been discussed in Section 3.2. The FTIR data have been converted into absorption spectra for both LCC and LSC samples and represented in Figs. 3 and 4, respectively. Fig. 5 shows
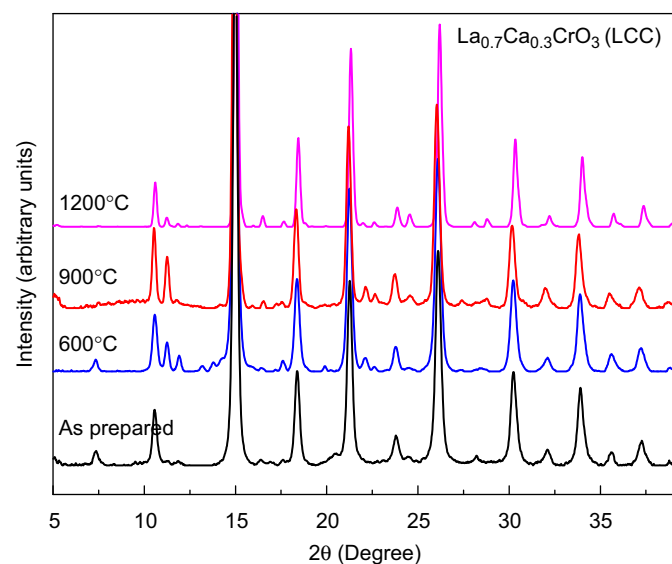

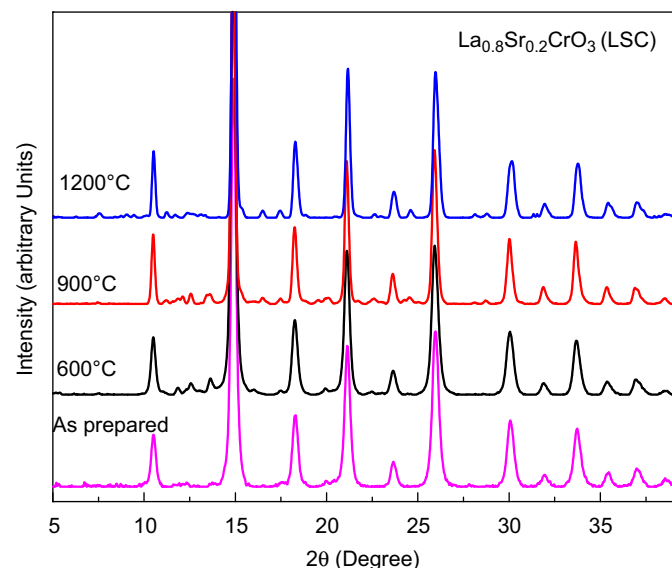**Fig. 1.** X-ray diffraction patterns of LCC calcined at various temperatures.

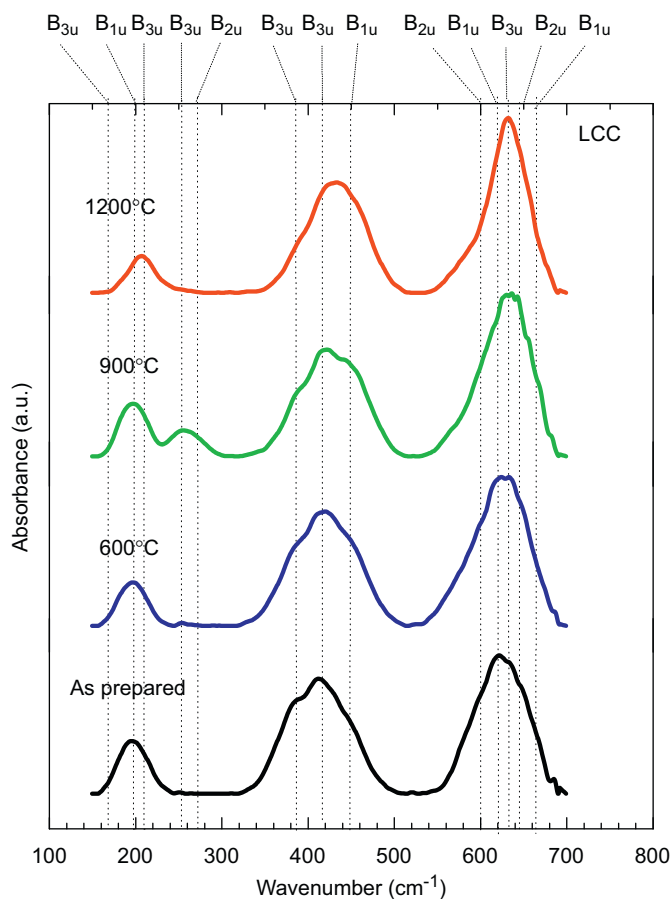**Fig. 2.** X-ray diffraction patterns of LSC calcined at various temperatures.

Fig. 3. FTIR spectra of LCC specimens from 150 to 700 cm^{-1}. Spectra have been offset along y-axis to avoid overlap and make the visualization clear.

the behavior of vibrational bands and Figs. 6 and 7 show the spectra in the extended frequency region which marks the evolution of intermediate phases.

3.1. FTIR spectroscopy

From Figs. 3 and 4, three broad absorption bands in the frequency range 670–570 (high frequency), 480–350 (mid-frequency) and at 190 cm^{-1} (low frequency) have been observed. These IR modes have been found similar to those of the orthorhombic perovskite LaCrO$_3$ (D$_{2h}^{16}$) with Pnma symmetry [19,20,38]. The irreducible representation of the optical modes [38], for ABO$_3$ structured compounds (A=rare-earth element and B= transition metal) with orthorhombic phase predicts 25 (7B$_{1u}$+9B$_{2u}$+9B$_{3u}$) IR active modes. The observed modes have been shown in dotted lines in Figs. 3 and 4. The lack of multiplicity, i.e. the observation of less number of modes compared to the predicted number of 25, can be due to the superposition of many modes very near to each other or small oscillator strengths of some of the modes. As discussed earlier, the dominant character of these IR modes is grouped into three types of vibrations, i.e. stretching, bending and external vibrations, respectively, which is more like the higher symmetry Pm3m cubic vibrations that have only three IR active phonon bands [39]. The effects of calcination temperatures on the three bands and signatures of intermediate phases have been discussed in following subsections.

3.1.1. High-frequency band

The high-frequency band spans the region from 570 to 670 cm^{-1}. This band arises mainly due to Cr–O–Cr asymmetric stretching of CrO$_6$ octahedron [19]. It has been well established that
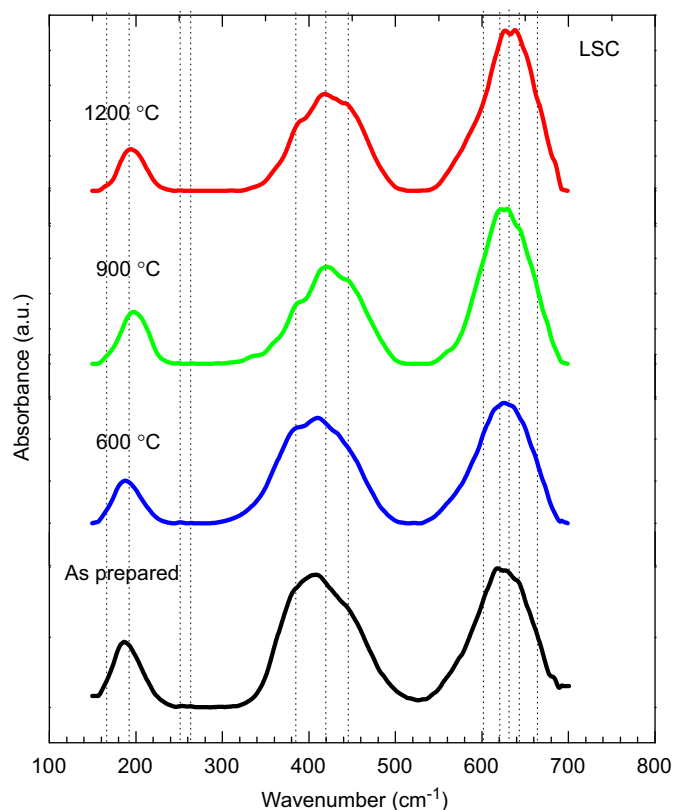
Fig. 4. FTIR spectra of LSC specimens from 150 to 700 cm^{-1}. Spectra have been offset for clarity.

the frequency of this mode is inversely proportional to bond length d_{Cr-O} [18]. The cell volume is proportional to the third power of d_{Cr-O} and cosine of the tilt angle [40]. Doping induced disorder due to the changed mass, charge and lattice parameters broadens the bands. A detailed study on variation of this high-frequency band with change of B site dopant has been carried out and it was shown that large octahedral field stabilization energies could lead to higher stretching frequencies [41]. The Cr–O stretching band appears at 630 cm^{-1} for LaCrO$_3$ [19]. It has been observed from Figs. 3 and 4 that the stretching vibrations shift towards lower frequencies upon Sr or Ca substitution. Shoulders in the spectra may imply the existence of several modes residing inside. Apart from strong B_{3u} (in-plane oxygen vibration; 630 cm^{-1}) and B_{2u} (apical oxygen vibration; 640 cm^{-1}), shoulders at 602 (B_{2u}) and 621 cm^{-1} (B_{1u}) have been observed. The shoulder in the spectra at nearly 665 cm^{-1} can be assigned to a combination band (B_{1u}) of O–Cr–O bending vibrations, which appears at 675 cm^{-1} for LaCrO$_3$ [19]. For LSC specimens, the Cr–O stretch band shifts towards higher frequency with increasing calcination temperature, as shown in Fig. 5. This rise in bond energy implies that the Cr–O bond length decreases with increasing temperature. B_{3u} (630 cm^{-1}) is prominent in all the samples, but B_{2u} (640 cm^{-1}) is split in high temperature calcined samples. For LCC specimens also, this peak shows a blue shift as the calcination temperature is increased. But the frequency increased considerably from 600 to 900 °C. This indicates that there is a difference in the behavior of microscopic structure at different temperatures for Sr- and Ca-doped samples, and that the temperature range across 900 °C is crucial for comparison of these two doped nano-ceramics. At 600 °C, the peak position of LCC ($\sim$623.5 cm^{-1}) is lower than LSC ($\sim$624.5 cm^{-1}), but as the temperature is increased to 900 °C, the peak position of LCC reaches nearly 630 cm^{-1}, whereas for LSC it is nearly 627 cm^{-1}, thus a larger reduction of Cr–O bond for LCC than LSC at the same higher temperatures of calcination. Though the reduction in Cr–O bond length may suggest a decrease in the unit cell
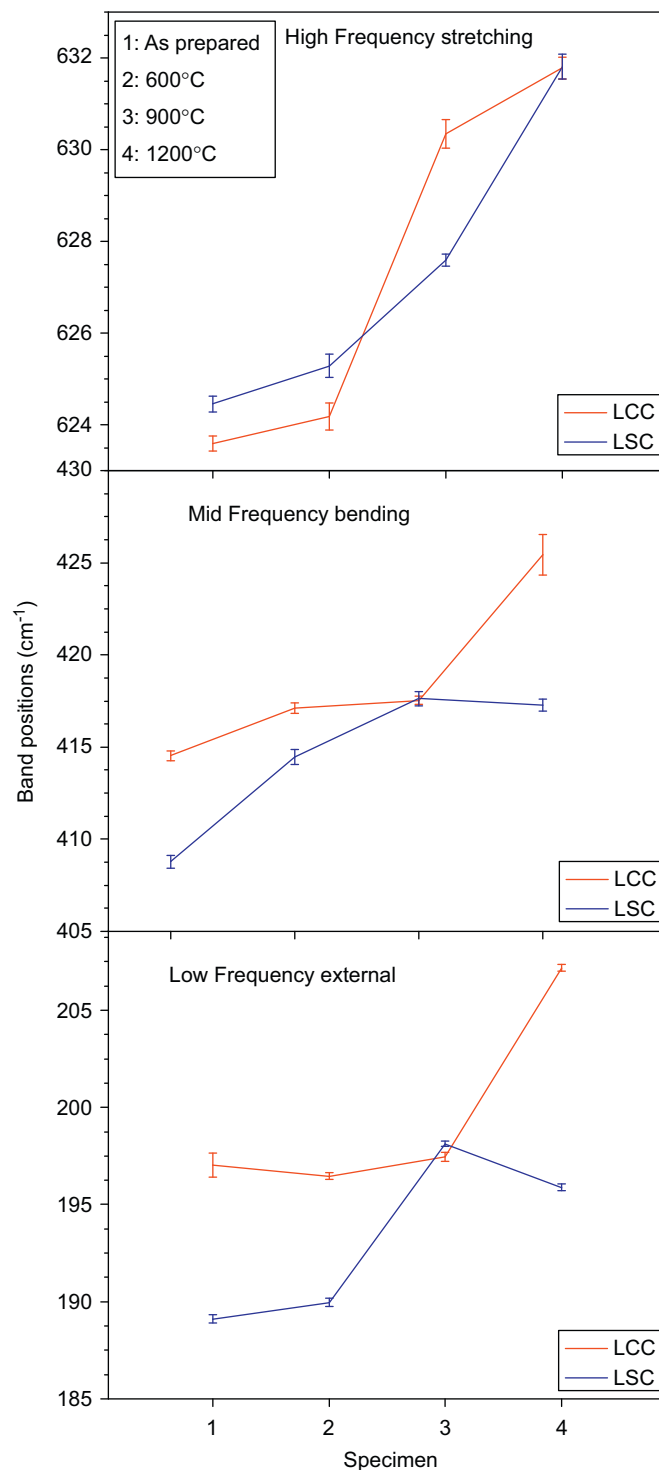

Fig. 5. Behavior of different vibrational bands of LCC and LSC with calcination temperature.

volume, but the XRD data show that the unit cell volume increases with increasing calcination temperature (Table 1). This may be due to the reduction in the tilt angle with temperature and would thus compensate for the reduction in the bond length. Implications of Table 1 will be discussed in a later section.

3.1.2. Mid-frequency band

The moderately strong mid-frequency band is again a superposition of many modes and is spread from 350 to 480 cm^{-1}.
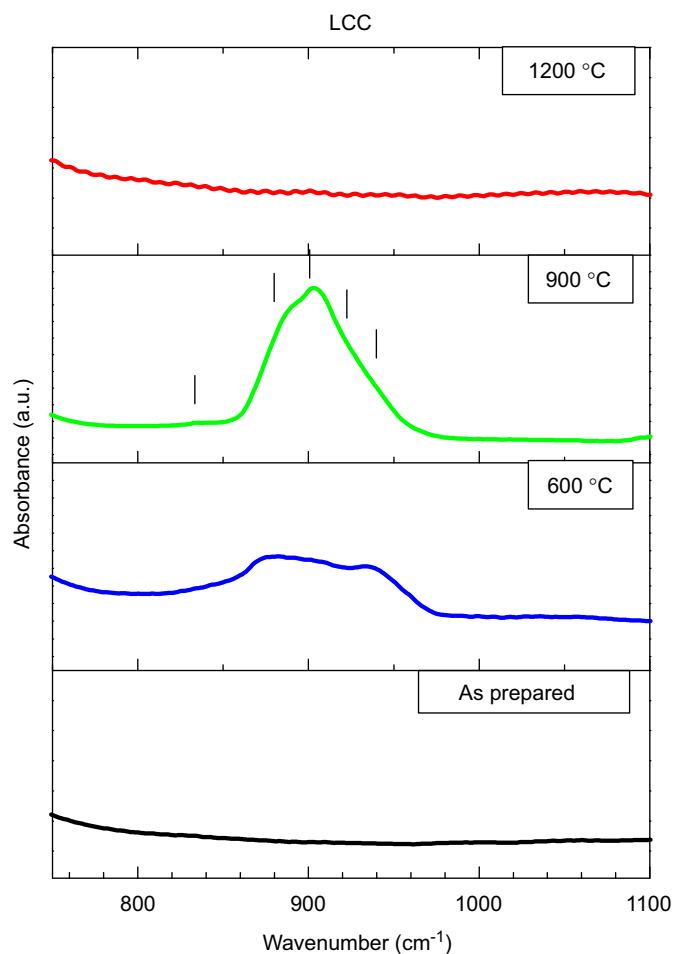
Fig. 6. IR spectra of LCC specimens from 700 to 1100 cm^{-1} showing CaCrO$_4$ modes appearing after the high frequency stretching modes of LCC.

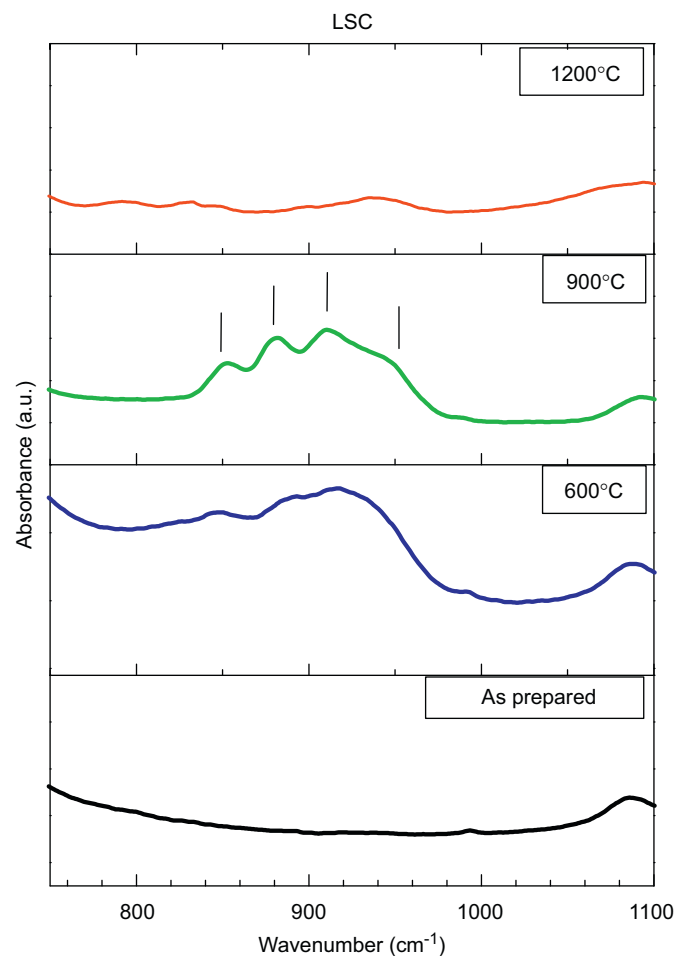**Fig. 7.** IR spectra of LSC specimens from 700 to 1100 cm^{-1} showing SrCrO$_4$ modes appearing after the high frequency stretching modes of LSC.

These modes arise due to the deformations of CrO$_6$ octahedron. For LaCrO$_3$, various O–Cr–O bending modes which are responsible for this broadband have been reported [20]. Apart from weak shoulders, three strong features are visible in the spectra shown in Figs. 3 and 4, which have been identified as B_{1u} (apical oxygen vibration; at 445 cm^{-1}), B_{3u} (in plane oxygen vibration; at 410 cm^{-1}) and B_{3u} (at 380 cm^{-1}) by comparison with the previously reported band positions for LaCrO$_3$ [18,20]. It is interesting to mention that for the doped perovskite compounds, the bending vibrations are proportional to and are predominantly governed by the bond length d_{La-O} [42]. Moreover, this mode is also inversely proportional to the La(Sr/Ca) site cation radius. The two B_{3u} modes correspond to bands at 425 and 380 cm^{-1} for LaCrO$_3$ [20]. The LSC frequencies for these internal bending vibrations are at slightly lower values compared to LCC, as depicted in Fig. 5. This is due to the larger ionic radius of Sr than Ca, which confirms the dependence of the bending mode on the dopant ionic size. For LSC specimens, frequencies gradually increase from as-prepared sample to 900 °C calcined sample. At 1200 °C calcination, there is a slight decrease in the frequency. These observed trends imply that the La–O bond length increases as the calcination temperature increases, but it again reduces slightly at temperatures more than 900 °C. For LCC samples, the band positions and hence La–O bond length first increases from as-prepared sample to 600 °C calcined sample. From 600 to 900 °C calcined sample, the shift in the frequency is very small, which again increases from 900 to 1200 °C calcined sample. Interestingly, the frequencies for the

two doped systems are very close at 900 °C, where the intermediate phases show prominent presence, discussed in a later section. Moreover, low frequency bending modes B_{2u} (265 cm^{-1}) and B_{3u} (240 cm^{-1}) are either very weak or not at all present in most of the samples except for the 900 °C calcined LCC sample, where B_{3u} (257 cm^{-1}) has emerged very strongly. There exists a weak shoulder at around 517 cm^{-1} for as-prepared and 600 °C calcined samples only of LCC, which can be explained as a defect band due to distortions of CrO$_6$ octahedron by the high valence cations. This weak band completely vanishes at higher calcination temperatures, implying a decrease in the structural disorder at higher calcination temperatures.

3.1.3. Low-frequency band

External modes arising from the La vibrations are expected to be present in the low frequency regions of the infrared spectrum, owing to higher mass of lanthanum. These modes occur due to a relative motion of the CrO$_6$ octahedra against the surrounding La(Sr/Ca) atoms. Five IR-active modes are expected to be present in the far infrared region from 100 to 200 cm^{-1} [38]. In fact, in present infrared spectrum, Figs. 3 and 4, from 150 to 200 cm^{-1}, a sharp band is observed peaked at around 200 cm^{-1} (B_{1u}) with a weak shoulder at nearly 165 cm^{-1} (B_{3u}). The frequency of the external mode is blue shifted at higher temperatures, as shown in Fig. 5, which can be attributed to the increased force constants and higher

Table 1
Extracted parameters from fitting of XRD data of LCC and LSC.

Calcination temperature	wt% of CaCrO$_4$	wt% of SrCrO$_4$	Unit cell vol. of La$_{0.7}$Ca$_{0.3}$CrO$_3$ (Å^3)	Unit cell vol. of La$_{0.8}$Sr$_{0.2}$CrO$_3$ (Å^3)
As-prepared	0	0	228.767	232.609
600 °C	10.4	12.5	229.138	233.153
900 °C	13.8	10.1	230.629	233.584
1200 °C	4	0.04	226.514	231.527

bond strengths for higher calcination temperatures. The frequencies are again closer at 900 °C for the two systems.

3.2. Intermediate phases

Spectra of the as-prepared samples of both Ca- and Sr-doped samples resemble that of pure LaCrO$_3$. But as the calcination temperature is increased, intermediate phases start appearing. The signatures of intermediate phases in the IR spectra have been identified by the stretching modes of CaCrO$_4$ in LCC and SrCrO$_4$ in LSC, as depicted in Figs. 6 and 7, respectively. The internal modes, i.e. stretching and bending vibrations, of these compounds lay in the far infrared region, i.e. below 1000 cm^{-1}. Though the bending vibrations, near 350–400 cm^{-1}, are overlapped by the La(Sr/Ca)CrO$_3$ internal bending modes, the stretching vibrations are well away from the overlap and are clearly visible for the samples for which the phase has appeared. The interesting observation from the present IR study is not only the evolution and disappearance of transient phases but also the absorption intensity of these phases, especially for LCC, is comparable to the native perovskite intensities. The formation of these phases has also been confirmed with the X-ray diffraction studies on the LCC and LSC compounds. After carrying out the refinement on the XRD data, the weight percentages of the intermediate phases and volume of the unit cell have also been calculated and have been tabulated in Table 1. The weight percent of the dopant chromate phases have been fitted using a quadratic function as shown in Fig. 8, and the as-prepared sample has been taken at room temperature for plotting the curves in Fig. 8.

CaCrO$_4$ (D_{2h}^{11}) crystallizes in the Pbcm space group. The stretching modes are expected to be present between 850 and 950 cm^{-1}, whereas bending modes are present at around 380 cm^{-1}. In a recent study, the stretching IR modes have been reported at 924, 912, 902, 870 and 850 cm^{-1} [43]. For LCC specimens, calcined at intermediate temperatures, the stretching modes have been observed near 840, 880, 903, 920 and 938 cm^{-1}, as shown in Fig. 6, which are in reasonable agreement with the reported data of pure compounds. Remarkably, the intensity of this band for 900 °C calcined specimen is comparable to those of the perovskite vibrations. There are no such peaks in the as-prepared sample, whereas their signature can be seen as a broadband for 600 °C calcined sample. But the peaks are not sharp enough and well split. For 900 °C calcined sample, there is a very strong and sharp band, peaked at 903 cm^{-1} and shoulders on either side. No such signature has been observed for the 1200 °C calcined sample. Analysis of the XRD data showed maximum CaCrO$_4$ phase formation at around 864 °C (Fig. 8), whereas 1200 °C calcined sample contains very small amount of CaCrO$_4$. These observations imply that the formation of CaCrO$_4$ started just below 600 °C with completely stabilized phase formation at some intermediate temperature near 900 °C. But, if the calcination temperature is further increased, these are dissolved back into the system. Thus, we may conclude that the disappearance of this phase starts after 900 °C where a broad intense IR band exists. It gets completely dissolved at temperature slightly higher than 1200 °C.
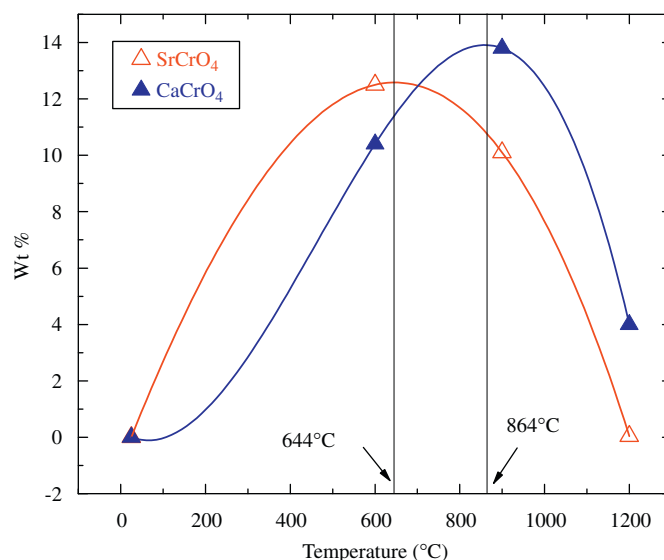
Fig. 8. Variation of weight percentage of the intermediate phases with respect to calcination temperature, obtained by fitting the XRD data. Solid vertical lines mark the position of maximum wt%.

SrCrO$_4$ (C_{2h}^5) with $P2_1/n$ space group, also has its stretching and bending vibrational modes present at similar frequencies. The stretching IR modes have been reported at 925, 912, 890, 875 and 843 cm^{-1} [43]. Interestingly, the infrared spectrum of LSC specimen, Fig. 7, calcined at 900 °C shows nearly all of these frequencies with clear and distinct peaks at 850, 880, 912 and 950 cm^{-1} and others as shoulders unlike as in LCC. In LSC also, there are no impurity phase features present in the as-prepared sample which again resembles to that of the pure LaCrO$_3$. The features of intermediate phase appear in the infrared spectrum of 600 and 900 °C calcined samples. Fitted XRD data show that the maximum SrCrO$_4$ phase formation takes place at around 644 °C (Fig. 8). These observations again depicted that sintering mechanism in LSC is different from LCC, in the sense that for LSC, the intermediate phase formation starts at relatively lower temperature below 600 °C, which starts dissolving at temperature between 600 and 900 °C. At 1200 °C, it vanishes almost completely.

From the infrared spectroscopic analysis, it has been noticed that vibrations involving the cation La(Sr/Ca), i.e. the internal bending modes and the external modes, show similar trends on increasing the calcination temperature. These LSC and LCC frequencies are very close to each other at 900 °C, where the intermediate phase has completely formed. It implies that the La–(CrO$_6$) structural units are similar to each other at around 900 °C calcination temperatures for both LCC and LSC, and the structure of the left out system, after the exsolution of some of the dopants as chromates, should be more like the pure LaCrO$_3$ system. From 900 to 1200 °C, when the intermediate phase dissolves back into the perovskite, the original structure is regained with LCC frequencies higher than LSC frequencies, but with sufficiently higher values than the as-prepared powders. This difference in

the frequencies was not noticeable at lower calcination temperature, i.e. between as-prepared to 600 °C calcined samples. These observations suggest that the microscopic structure gets significantly modified during the process of the formation and dissolution of the intermediate phases. The argument is more supportive, if we look at the behavior of internal stretching modes involving only pure CrO_6 cages, where the frequencies gradually increase on increasing the calcination temperature showing faster rise in the regime of intermediate phase formation. At 1200 °C the frequencies are close to each other and are sufficiently higher than the as-prepared powder. Thus temperature range across 900 °C is crucial and the microscopic structure gets modified due to the evolution of impurity phases at intermediate temperatures. For 1200 °C calcination temperature, although the structures are similar to as-prepared samples, i.e. with practically no dopant phases, but the frequencies have been enhanced showing stronger bond strengths for higher temperature calcined samples. Another striking feature is that at 900 °C, for LCC, more number of splitted modes is observed, which more like a pure orthorhombic character is. The effects of intermediate phase formation on the microscopic structure of LSC is smaller as compared to that of LCC which may be attributed to the lower extent of doping, as the relative intensity of the IR peaks of $CaCrO_4$ are more than $SrCrO_4$ implying lesser formation of the $SrCrO_4$, or lower buckling of octahedra along the b-axis for LSC than LCC, as the $Pnma$ unit cell can be obtained from the cubic one by a combined rotation of the octahedra along the (1 0 0) and (1 1 0) direction resulting in a buckling of the octahedra along the b-axis [44].

3.3. SANS data analysis and discussion

SANS data have been represented in absolute scale for both LCC and LSC samples and have been plotted in Figs. 9 and 10, respectively. SANS profiles for LCC specimens (Fig. 9), show power law behavior in certain q-range, indicating a fractal type correlation of the aggregates. Fractal correlation gets modified with increasing calcination temperature. It is also evident from the profiles that a hump like structure appears at high q ($q \sim 0.09$ nm^{-1}), which is pronounced at lower calcination temperatures. The appearance of such hump-like feature is attributed to the hard sphere type correlation of the primary particles. Power law behavior in SANS profiles has also been observed for LSC samples (Fig. 10). It has been observed that SANS profiles for
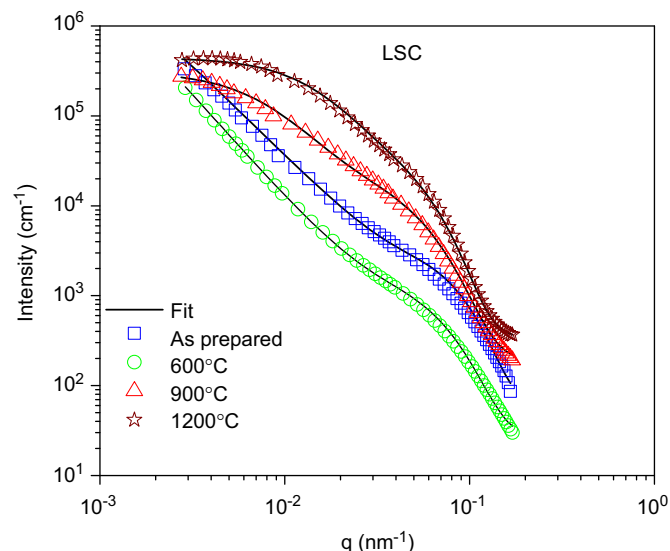

Fig. 10. SANS scattering profiles at different calcination temperatures for the LSC samples.

both LCC and LSC powders are best described by accounting the fractal and hard sphere type correlation of the primary particles of the aggregate

$$\frac{d\sum}{d\Omega}(q) = c_1 \left[\int_0^\infty v_p^2(r)P(q,r)D(r)S_{HS}(q,r,\eta)dr \right.$$
$$\left. + c_2 \int_0^\infty v_p^2(r)P(q,r)D(r)S_{Fractal}(q,r,\xi)dr \right] \qquad (1)$$

where c_1 and c_2 are the q independent scale factors, $v_p(r)$ is the volume of primary particle with radius r and $P(q, r)$ is the form factor of the particle. In the present case spherical form factor has been adopted for data analysis as it could best fit our data and is given as

$$P(q) = 9\left[\frac{\sin(qR) - qR\cos(qR)}{(qR)^3}\right]^2 \qquad (2)$$

S_{HS} (q, r, η) is hard sphere structure factor [45] to account high q correlation ($q \sim 0.09$ nm^{-1}) of the primary particles in the present q window, where η is the volume fraction of the primary particles. $S_{Fractal}(q,r,\xi)$ is structure factor to account the mass fractal correlation [26,27] at lower q range. ξ is the upper cutoff length of the fractal aggregate and represents the length scale up to which fractal correlation exists. $D(r)$ is particle size distribution. In the present case log-normal distribution has been taken as

$$D(r,a,b) = \frac{1}{\sqrt{2\pi b^2 r^2}} \exp\left[-\frac{\{\ln(r/a)\}^2}{2b^2} \right] \qquad (3)$$

where a and b are the parameters representing the median and polydispersity index of the distribution. The size distributions of the primary particles for both LCC and LSC have been depicted in Figs. 11 and 12, respectively. It is evident from the figures that the primary particle size increases with increasing calcination temperature indicating the coalescence of smaller particles to form bigger particles. Important parameters, extracted from fitting to the scattering data for LCC and LSC samples, are shown in Tables 2 and 3, respectively.

From Fig. 11 and Table 2, it is clear that agglomerates in as prepared LCC powder possess a mass fractal like morphology with a mass fractal dimension (D_F) of 2.2 and upper cutoff length 221 nm. These fractal agglomerates consist of primary particles with an average radius 15.8 nm. This indicates that the fractal agglomerates
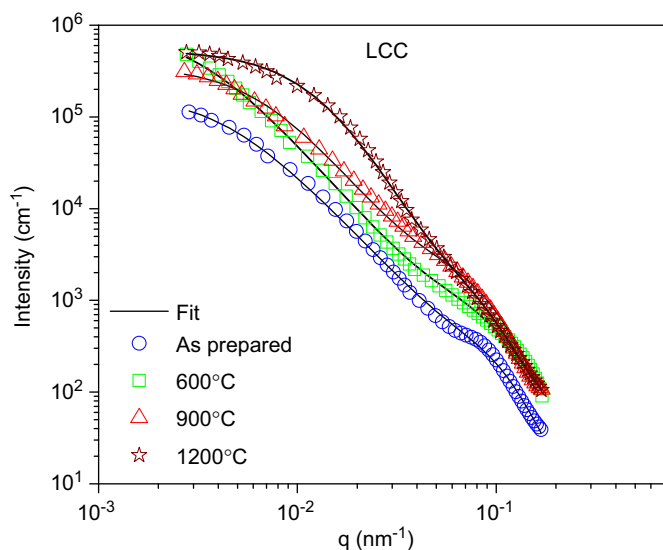

Fig. 9. SANS scattering profiles at different calcination temperatures for the LCC samples.

of initial precursor powder are very loose. Fractal dimension (D_F) of agglomerates increases towards ~2.9 with increasing calcination temperature. Further, the upper cutoff of the fractal decreases significantly at higher temperatures. These modifications below calcinations temperature of 900 °C may be attributed to the compaction of the fractal aggregates via diffusion during sintering process at lower calcination temperature. However, it is interesting to note that fractal dimension increases considerably, to 2.9, when
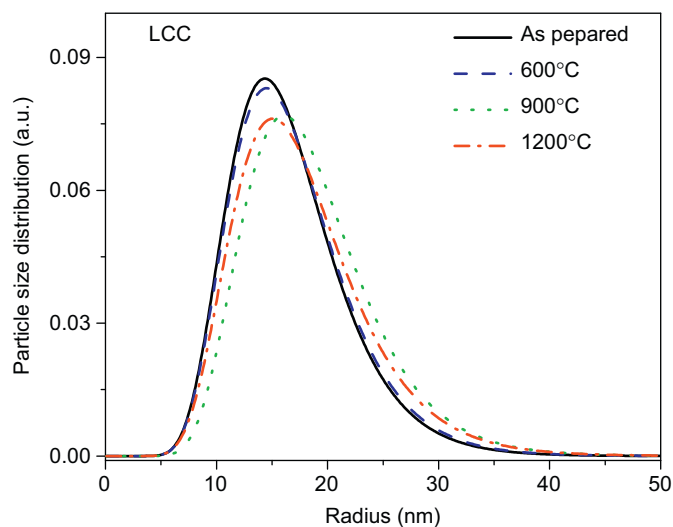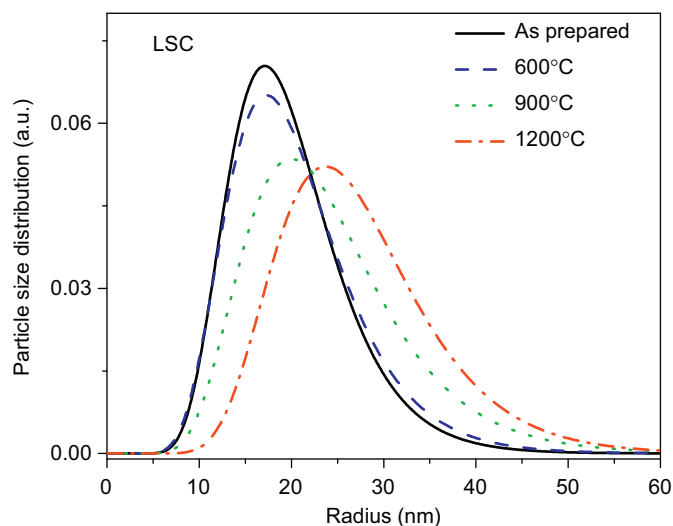
calcination temperature is increased beyond 900 °C. This shows that the agglomerates, which are loose in nature at lower temperature, start getting compacted at higher calcination temperatures. It is interesting to note that the diffusion mechanisms at lower calcination temperatures may be grain boundary diffusion. However, around and beyond 900 °C, due to the formation of intermediate phases by the melting of dopant chromates, as supported by FTIR studies, the diffusion is dominated by viscous flow of the material that leads to faster densification and thus compaction of aggregate.

Similar observations have been realized for the LSC specimens except for some quantitative differences. From Fig. 12 and Table 3, it is clear that the structure of the agglomerate in as prepared LSC powder also possesses a mass fractal morphology but with a mass fractal dimension of 2.0 and an upper cutoff length more than 1000 nm that is beyond present SANS instrumental resolution. The size of the primary particles was found to be approximately 19 nm. It is clear that upper cutoff is significantly larger for as-prepared powder of LSC in comparison to that of LCC. Furthermore, the average size of the primary particles for LSC is somewhat larger than that for LCC powders. In addition, the position of the hump in the scattering profile due to the presence of interparticle interference differs in virgin LSC and LCC powders. These comparisons also indicate that agglomerates in initial virgin powder of LSC possess relatively loose structure and is also larger as compared to that of LCC. Further, from the difference in agglomeration nature of LCC and LSC, it appears that the sintering of LCC virgin powder is relatively easier as compared to that of LSC in spite of their iso-structural phase.

Fig. 11. Primary particle size distributions of the LCC aggregate with calcination temperature.

3.3.1. Scanning electron microscopy (SEM)

To verify the mesostructural modifications during calcination of the specimens, obtained by scattering data, scanning electron microscopy (SEM) has also been carried out. It is noteworthy to mention here that microscopy is a direct method to observe the mesoscopic length scale; however it is local probe of the matter. The SANS is an indirect method to see the mesoscopic length scale and is a bulk sensitive technique. The information extracted by scattering is statistically averaged over bulk of the specimen. In general, microscopy and scattering methods are used as complimentary techniques to probe the mesoscopic length scale.

To observe the modifications in the agglomerates during calcination, SEM micrographs of the as-prepared and calcined specimens of both LSC and LCC have been shown in Figs. 13 and 14, respectively. As predicted, the agglomerates of the as-prepared specimens are very loose. It is also evident from the images that the overall agglomerate size decreases and the agglomerates get compacted with increasing calcination temperature. These observations corroborate with SANS results, as fractal dimension of the agglomerates increases towards the Euclidean dimension (D_f=3) and also the fractal upper cutoff length decreases with increasing calcination temperature (Tables 2 and 3).
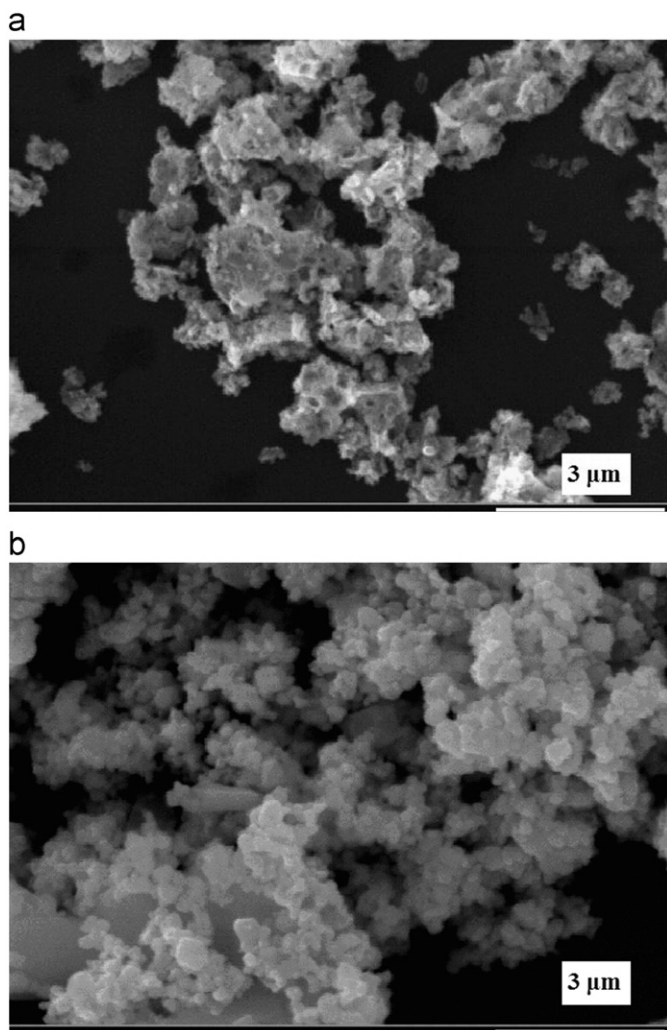

Fig. 12. Primary particle size distributions of the LSC aggregate with calcination temperature.

Table 2
Extracted parameters from model fitting to the LCC data obtained by SANS.

| Calcination temperature	Fractal dimension (D_f)	Mean radius (nm)	Polydispersity index (b)	Upper cutoff ξ (nm)
As-prepared	2.2	15.8	0.3	221
600 °C	2.3	16.0	0.3	294
900 °C	2.5	17.7	0.3	144
1200 °C	2.9	16.8	0.3	73

Table 3
Extracted parameters from model fitting to the LSC data obtained by SANS.

Calcination temperature	Fractal dimension (D_f)	Mean radius (nm)	Polydispersity index (b)	Upper cutoff ξ (nm)
As formed	2.0	18.9	0.31	–
600 °C	2.3	19.3	0.33	–
900 °C	2.5	22.6	0.35	118
1200 °C	2.9	26.0	0.30	52

Fig. 13. SEM images of the (a) as-prepared and (b) 1200 °C calcined LSC specimens.
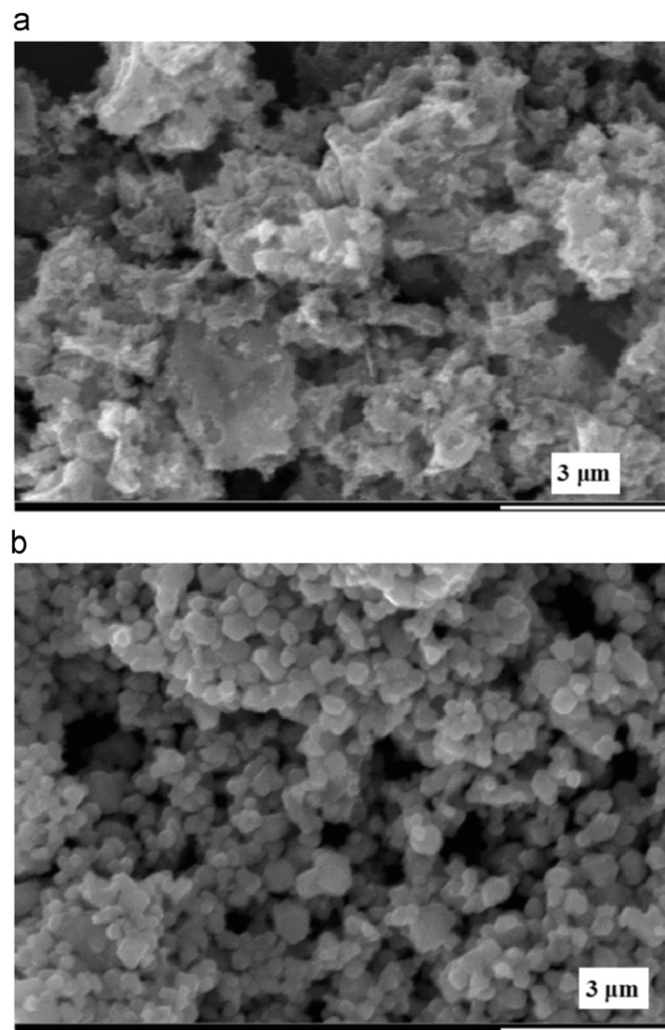
Fig. 14. SEM images of the (a) as-prepared and (b) 1200 °C calcined LCC specimens.

4. Conclusions

For LCC and LSC, IR active vibrations are mostly confined in three broad absorption bands. Evolution of intermediate phases ($CaCrO_4$ for LCC and $SrCrO_4$ for LSC) takes place as the calcination temperature is increased, which have been detected by their characteristic IR active stretching vibrational modes and confirmed by the X-ray diffraction data. The whole process of evolution and disappearance of intermediate phases takes place at lower calcination temperatures for Sr-doped chromites. During calcination at intermediate temperatures, the decrease in Cr–O stretch, increase in La–O bond length and decrease in tilt angle results in increase in the unit cell volume. Thus, the microscopic structure of the systems get modified with calcination temperature in the regime of intermediate phase formation, which is regained at higher temperatures where the dopant chromates get redissolved into the original structure, but with sufficiently higher bond strengths. While the vibrational studies manifest mainly about the microscopic structure of the composites, neutron scattering results enlighten the mesoscopic nature. The bridge between the two studies is the possibility of the occurrence of the phenomenon of liquid state assisted sintering through the melting of intermediate phases. It has been noticed that not only the microscopic, but the mesoscopic structure of the nano-ceramics also gets significantly modified with calcination temperature. Fractal dimension and cutoff lengths of the agglomerates get altered at higher temperature leading to compaction of the agglomerates. This is attributed to liquid state assisted sintering at intermediate temperatures. The temperature regime across 900 °C emerges as crucial range for the comparison of the two doped nano-crystalline perovskites as well as for the sintering mechanisms in the two systems.

Acknowledgment

References

[1] B.C.H. Steele, A. Heinzel, Nature 414 (2001) 345.
[2] M. Gasik, Materials for Fuel Cells, Woodhead Publishing, 2008.
[3] M. Mori, T. Yamamoto, H. Itoh, T. Watanabe, J. Mater. Sci. 32 (1997) 2423.
[4] X.J. Chen, Q.L. Liu, N.P. Brandon, K.A. Khor, Fuel Cells Bull. 6 (2007) 12.
[5] L.L. Zhang, Review, MSE 04053/CISM/11z, 2004.
[6] T. Nakamura, G. Petzow, L.J. Gauckler, Mater. Res. Bull. 14 (1979) 649.
[7] O. Yamamoto, Electrochem. Acta 45 (2000) 2423.
[8] B.F. Flandemeyer, M.M. Nasrallah, D.M. Sparlin, H.U. Anderson, High-Temp. Sci. 20 (1985) 265.
[9] H.C. Graham, H.H. Davis, J. Am. Ceram. Soc. 54 (1971) 89.
[10] H. Yokokawa, N. Sakai, T. Kawada, M. Dokiya, J. Electrochem. Soc. 138 (1991) 1018.
[11] L.A. Chick, J. Liu, J.W. Stevenson, T.R. Armstrong, D.E. McCready, G.D. Maupin, G.W. Coffey, C.A. Coyle, J. Am. Ceram. Soc. 80 (1997) 2109.
[12] T.R. Armstrong, J.W. Stevenson, L.R. Pederson, P.E. Raney, J. Electrochem. Soc 143 (1996) 2919.
[13] L.A. Chick, J.L. Bates, G.D. Maupin, in: F. Grosz, P. Zegers, S.C. Singhal, O. Yamamoto (Eds.), Proceedings Second International Symposium on Solid Oxide Fuel Cells, Athens, Greece, 1991, p. 621.
[14] S. Simner, J. Hardy, J. Stevenson, T. Armstrong, J. Mater. Sci. 34 (1999) 5721.
[15] N.M. Sammes, R. Ratnaraj, M.G. Fee, J. Mater Sci. 29 (1994) 4319.
[16] D.B. Meadowcroft, J. Brit., Br. J. Appl. Phys. Ser. 2 (1969) 1225.
[17] M. Mori, Y. Hiei, N.M. Sammes, Solid State Ionics 123 (1999) 103.
[18] R.K. Gupta, C.M. Whang, Solid State Ionics 178 (2007) 1617.
[19] G.V.S. Rao, C.N.R. Rao, J.R. Ferraro, Appl. Spectrosc. 24 (1970) 436.
[20] G.A. Tompsett, N.M. Sammes, J. Power Sources 130 (2004) 1.
[21] I.S. Smirnova, Physica B 262 (1999) 247.
[22] A.K. Patra, J. Bahadur, S. Mazumder, S. Nair, R.D. Purohit, A.K. Tyagi, J. Nanoscience Nanotechnology 8 (2007) 1.
[23] J. Bahadur, D. Sen, S. Mazumder, R. Shukla, A.K. Tyagi, J. Phys.: Condens. Matter 20 (2008) 345201.
[24] J. Bahadur, D. Sen, S. Mazumder, S. Ramanathan, J. Solid State Chem. 181 (2008) 1227.
[25] D. Sen, J. Bahadur, S. Mazumder, V. Bedekar, A.K. Tyagi, J. Phys.: Condens. Matter 20 (2008) 035103.
[26] J. Teixeira, J. Appl. Cryst. 21 (1988) 781.
[27] T. Freltoft, J.K. Jems, S.K. Sinha, Phys. Rev. B 33 (1986) 269.
[28] C. Orr, Powder Technol. 3 (1969) 117.
[29] K. Ishizaki, S. Komarneni, M. Nanko, Porous Materials: Process technology and applications, vol. 202, Kluwer Academic Publishers, Dordrecht, The Netherlands, 1998.
[30] B.B. Mandelbrot, The fractal geometry of nature, Freeman, New York, 1983.
[31] A. Guinier, G. Fournet, Small-angle Scattering of X-rays, John Wiley and Sons, Inc, New York, 1955.
[32] L.A. Feigin, D.I. Svergun, Structure analysis by small-angle X-ray and neutron scattering, Plenum, New York, 1987.
[33] G. Kostorz, Treatise on Materials Science and Technology, vol. 15, Academic Press, New York, 1979, p. 227.
[34] OPUS, Bruker Optik GmbH, Germany Version 6.0, 2006.
[35] S. Mazumder, D. Sen, T. Sarvanan, P.R. Vijayraghavan, J. Neutron Research 9 (2001) 39.
[36] P.W. Schmidt, R. Height, Acta. Crystallogr. 13 (1960) 480.
[37] J.A. Lake, J. Appl. Cryst. 23 (1967) 191.
[38] M. Daturi, G. Busca, R.J. Willy, Chem. Mater. 7 (1995) 2115.
[39] F. Mayr, Ch. Hartinger, A. Loidl, Phys. Rev. B 72 (2005) 024425.
[40] P.G. Radaelli, G. Iannone, M. Marezio, H.Y. Hwang, S.W. Cheong, J.D. Jorgensen, D.N. Argyriou, Phys. Rev. B 56 (1997) 8265.
[41] P. Ganguly, N.Y. Vasanthacharya, J. Solid State Chem. 61 (1986) 164.
[42] L. Martin-Carron, A.D. Andres, M.J. Martinez-Lope, M.T. Casais, J.A. Alonso, Phys. Rev. B 66 (2002) 174303.
[43] D. Stoilova, M. Georgiev, D. Marinova, Vib. Spectrosc. 39 (2005) 46.
[44] A.K. Bogush, V.L. Pavlov, L.V. Balyko, Cryst. Res. Technol. 18 (1983) 589.
[45] R.J. Baxter, J. Chem. Phys. 49 (1968) 2770.